Journal of Membrane Science 708 (2024) 122988

Contents lists available at ScienceDirect

Journal of Membrane Science

journal homepage: www.elsevier.com/locate/memsci

Full length article

Temporal resistance fluctuations during the initial filtration period of colloidal matter filtration

Lucas Stüwe [a,1], Arne Lüken [a,b,1], Felix Stockmeier [a,b], Lukas Griesberg [a], Timon Kratzenberg [c], John Linkhorst [a,d], Walter Richtering [c], Matthias Wessling [a,b,*]

[a] Chemical Process Engineering AVT.CVT, RWTH Aachen University, Forckenbeckstraße 51, Aachen, 52074, Germany
[b] DWI - Leibniz-Institute for Interactive Materials, Forckenbeckstraße 50, Aachen, 52074, Germany
[c] Institute of Physical Chemistry, RWTH Aachen University, Landoltweg 2, Aachen, 52074, Germany
[d] Process Engineering of Electrochemical Systems, Department of Mechanical Engineering, Technical University of Darmstadt, Otto-Berndt-Straße 2, Darmstadt, 64287, Germany

ARTICLE INFO

Keywords:
Soft matter filtration
Microgels
Fouling
Resistance fluctuations
Ultrafiltration

ABSTRACT

Membrane filtration processes with flux reversal for backwashing are employed to manage fouling during colloidal fluid treatment. This flux reversal accompanies filtration cycles where the total resistance increases over time. However, little is known about the initial phase of filtration. We focus on early filtration phase and present a microfluidic filtration system that allows precise observation of filtration resistances under constant flux or constant pressure operation for soft matter dead-end filtration with subsequent percolation of pure solvent. We identified temporal hydraulic resistance fluctuations during the start-up phase, which significantly differed from the steady-state condition. We focus on the experimental filtration of soft core–shell poly(N-isopropylacrylamide)-co-acrylic-acid microgels and observed a distinct peak in filter cake resistance with a subsequent reduction down to 50% of the initial peak resistance. To comprehend the phenomenon, we complement the experiments with temporal and spatial confocal microscopy studies linking cake compression and cake density gradients to its resistance. By comparing filtration, dialysis, and centrifugation as different microgel purification methods, we discover microgel shell degradation leading to detached polymer chains permeating in the downstream which causes the observed resistance reduction. This result demonstrates the permeation-induced degradation of macromolecular colloids during membrane filtration.

1. Introduction

The filtration of soft colloidal matter in micro- and ultrafiltration is a pivotal process in diverse fields. In water treatment, including water reuse of municipal wastewater, micro- (MF) and ultrafiltration (UF) are often used as pre-treatment for reverse osmosis to retain contaminants such as dust particles or cells in MF, or microbes and macromolecules in UF [1]. The application of MF and UF in food processing is a mild and energy-efficient separation method to remove microorganisms, proteins, and bacterial and protozoan pathogens [2–4]. In biotechnology, typical processes include 10 to 20 membrane-based purification steps crucial for retaining cells and cell debris via MF in the upstream and downstream for protein purification via UF [5]. One of the most common challenges in membrane processes is the decline of flux due to membrane fouling and the development of a filter cake. The filter cake accumulating on the membrane's surface adds an additional hydraulic resistance to the overall process and increases the energy demand for separation, deteriorating the overall process efficiency. Although micro- and ultrafiltration are widespread separation techniques, the phenomena and events that occur during filtration at the particle level still need to be discovered and understood [6]. Even though we have succeeded in predicting some phenomena of depth filtration [7] and cake layer build-up and rearrangements [8] using particle-based discrete element Computational Fluid Dynamics (CFD) simulations, the physics of membrane filtration remains challenging to describe comprehensively by experimental means. Existing macroscopic models for describing filter cake resistances in filtration processes are based on empirical expression with limited mechanistic understanding [9,10] and often rely on the filtration of solid particles. Most mechanistic models describing membrane filtration processes are based on Darcy's law, which correlates the permeate flux J to the

---

[*] Corresponding author at: Chemical Process Engineering AVT.CVT, RWTH Aachen University, Forckenbeckstraße 51, Aachen, 52074, Germany.
E-mail address: manuscripts.cvt@avt.rwth-aachen.de (M. Wessling).

[1] Authors contributed equally.

https://doi.org/10.1016/j.memsci.2024.122988
Received 19 April 2024; Received in revised form 4 June 2024; Accepted 8 June 2024

Transmembrane Pressure (TMP) ΔP by the permeate viscosity μ and the intrinsic membrane resistance to filtration R_m: $J = \Delta P/\mu R_m$ [11]. The resistance-in-series model expands Darcy's law by substituting the intrinsic membrane resistance with a total filtration resistance, which is often a sum of different resistances in series, such as pore blocking, filter cake and intrinsic membrane resistances [12]. The specific resistance for pore blocking can be obtained through the semi-empirical Hermia model [13], while the filter cake resistance can be derived using the Carman–Kozeny equation. Further studies suggest the differentiation between internal fouling due to pore blocking by soft matter and external fouling originating from filter cake formation [14].

However, most MF and UF applications feature the accumulation of soft matter. The soft and compressible filter cake complicates the purification process as, unlike assumed in the empirical models, colloids deform at elevated pressures, reducing the pore sizes in the cake and drastically increasing the hydraulic resistance [15,16]. This leads to a packing density gradient with higher porosity at the bulk side and a significantly compacted filter cake in the layers adjacent to the membrane. This pressure- and spatial-dependent effect is accounted for only through empirical correction factors in the existing models [17].

Albeit a challenging realistic implementation and the accompanying simplification necessary [18], visualization of the filtration process remains demanding to include mechanistic phenomena in improving filtration models. In recent years, microfluidics has emerged as a powerful tool to visualize and analyze particle deposition and particle interactions at the microscale [6,19,20]. Their unique ability to mimic real-world filtration conditions while providing unparalleled insights into the fundamental processes has opened new avenues for studying soft matter filtration on a particle scale. As an example, Agbangla et al. elucidated the dynamics of particle deposition forming arches at different filtration conditions in a microfluidic chip [21], a phenomenon that has been suggested earlier with diffusion-limited aggregation studies [22] and recently with CFD simulation coupled with Discrete Element Method model (CFD-DEM) [7,8]. Further investigations on the role of connectivity and tortuosity in a model membrane [23] and the formation of colloidal aggregation in the downstream can be found in the literature [24].

Microgels are often used as soft model particles due to their facile production and adjustable properties such as size, shape, softness, and charge to account for the soft material properties of the rejected colloidal matter, such as cells or protein aggregates during filtration. On a particle scale, microgels strongly deform at elevated pressures and even pass through pores with diameters much smaller than their own [25–28]. In an assembly of monodisperse microgels, asymmetric deformation can lead to crystalline colloidal filter cakes during filtration, decreasing the inter-particle voids and increasing resistance during filtration [16].

Further insights were derived through microfluidic filtration studies, emphasizing the importance of cake compression history on the soft filter's packing density. In particular, an already compressed filter cake featured a lower particle distance under similar filtration conditions and, therefore, a lower porosity than an uncompressed one [29]. In a later study, we could visualize the effects of rearrangement during compression and filter cake build-up and could correlate the share of irreversible compression [30].

Furthermore, the filtration behavior of microgels is intricately tied to their diverse properties, encompassing a broad spectrum of size and softness, both pivotal in filtration applications. Notably, the radial distribution of the crosslinking density within microgels results in a locally varied mechanical response to external forces. This distribution leads to a less crosslinked, softer corona and a stiffer particle core [31]. This effect has notable consequences when shearing microgels with radial crosslinking distribution in applications such as filtration, injection and extrusion. By integrating a force-responsive mechanofluorophore in poly(N-vinylcaprolactam) (PVCL) microgels, Izak-Nau et al. proved that the softer corona degrades rapidly, even at modest shear forces during needle extrusion. Such covalent bond scission further increased the lower the microgels were crosslinked [32]. They predicted that this rapid degradation of the coarsely crosslinked corona upon shear would severely impact on applications such as microgel filtration, a promising pathway for the purification of large-scale microgel productions by precipitation polymerization [33]. The shear stress encountered during purification significantly shapes the microgel's structure and properties in subsequent applications. For example, microgels purified through dialysis experience less shear stress compared to purification by filtration due to the different driving force, resulting in a softer structure with a more fuzzy corona. In a recent study, He et al. evaded shear-induced degradation of the outer shells of microgels through ultrasound by integrating a photoswitch into the polymer network. This shifts the volume phase transition temperature to lower temperatures, collapses the microgels, and cloaks them from degradation by external forces [34]. Such studies emphasize the non-inert behavior of microgels as model systems for soft matter filtration studies. Their polymer structure undergoes degradation in response to the shear forces inherent during filtration processes which result from fluid permeating the filter cake. These structural changes in the filter cake material can lead to initially inexplicable phenomena during filtration.

Despite the progress in visual insights during filtration and the behavior of the filter cake, which enhances the understanding of soft matter filtration, some phenomena reported in the literature remain inexplicable. One example is the so-called 'retarded packing compressibility', first described in 1953 by Rietema [35], where parts of a filter cake from polyvinyl chloride particles abruptly change their structure after the initial constant flux or constant pressure filtration leading to an unexpected increase in resistance. In addition, Tarleton et al. reported an accompanying increase in filtrate flow for the dead-end pressure filtration of an aqueous zinc sulfide suspension [36], being temporary and reversible. This phenomenon, which is not uncontroversial, has been attributed in a further study to discontinuities in the initial stage of constant flux filtration [37]. Fluctuations in the initial phase, such as reduced hydraulic resistance, were also briefly mentioned in microfluidic investigations with microgels as model particles [38] and in the sterile filtration of mRNA-lipid nanoparticles [39]. In the latter, the reduction in resistance is hypothesized to be attributed to an intrusion and break-through of the amorphous deposit of the colloids into the membrane, resulting in partly incomplete retention. However, a compelling explanation for the unexpected decrease in resistance has not yet been provided. This showcase underlines the potential of optical in-situ analysis of the filter cake during and after filtration to further refine the understanding of filtration processes and develop more profound explanations for variations of membrane resistance.

The present paper combines microfluidic visual observations with filtration data obtained from lab-scale microgel filtration to link membrane filtration phenomena to structural effects in the filter cake. In particular, we report resistance fluctuations during the start-up phase of microgel dead-end filtration with subsequent percolation of pure solvent under different conditions, such as flux, particle amount, and pressure. Based on in-situ observations and post-analysis of the microgels, we are able to link the observed resistance fluctuations to the degradation of the soft microgel corona and subsequent permeation of ruptured polymer chains through the filter cake into the permeate. Tracking labeled microgels during filtration allows us to rule out other effects, such as rearrangement of the microgels in the filter cake, as the cause of these resistance fluctuations. In fact, our investigations emphasize that shear forces originated from the permeating flow through the filter cake voids alter and degrade the microgel structure during shear-intense membrane filtration processes, which macroscopically causes temporal resistance fluctuations during the initial filtration period of colloidal matter filtration.

2. Experimental

2.1. Microgel synthesis

Three different types of colloids with different stiffness were filtrated with the filtration setup. Poly(N-isopropylacrylamide)-co-acrylic-acid core–shell microgels were synthesized batch-wise as described by Go et al. [40] with a mixture of N-isopropylacrylamide monomer (14 g/l), N,N'-methylenebisacrylamide (1 wt%) as crosslinker, potassium persulfate (5.8 wt%) as initiator and acrylic acid (7 wt%) in aqueous solution. All percentages are given relative to the monomer amount. The microgels' core is made from polystyrene (PS) labeled with Nile-red with a diameter of 200 nm, resulting in a mean microgel shell diameter of approx. 1.9 um (size distribution given in Fig. A.8, DLS-ZetaSizer Ultra, Malvern). The labeling enable the visualization of the microgels' position in the filter cake during filtration via confocal microscopy. As already reported in Lüken et al. [41], a zeta potential of −37 mV at pH 7 was measured (DLS-ZetaSizer Ultra, Malvern). After synthesis, the microgel solution was purified by dialysis (25kDa, SpectraPor 6, CarlRoth) against deionized water for seven days. The deionized water was exchanged twice a day. The microgel concentration in solution was $10\,\mathrm{mg\,mL^{-1}}$. As different microgel masses were injected in different experiments, the injected volume was adjusted accordingly.

Carbopol 934 (Lubrizol) is a highly versatile gelling agent from high molecular and cross-linked weight polymer of acrylic acid in powder form. It is extensively utilized across various industries due to its effective thickening and stabilizing properties [42]. The particle size of the powder is known from literature to range between 0.2 to $6\,\mathrm{\mu m}$ and swelling by a factor of about 10 in water [43]. In this study, it is used as an additional model system for soft hydrogels. The carbomer powder was dispersed in deionized water in small increments under constant mixing with a concentration of $1\,\mathrm{g\,L^{-1}}$ for 24 h.

Spherical monodisperse PS particles (FluoroMax, R500, Thermo Fisher Scientific) with a diameter of $2\,\mathrm{\mu m}$ and a density of $1.05\,\mathrm{g\,cm^{-1}}$ were used as stiff material system as comparison to the softer carbopol and microgel particles. The solution is supplied in an aqueous concentration of 1 wt% and injected at this concentration.

2.2. Microgel filtration

Soft poly(N-isopropylacrylamide) (pNIPAM) microgels, carbopol particles and PS particles were filtered inside a custom-made filtration module fabricated by additive manufacturing (VeroClear, J850 Pro, Stratasys) in dead-end operation with subsequent percolation. A pressure controller (PC) (Elveflow OB1 MK3+) is connected to a reservoir with a buffer feed that sets the transmembrane pressure (TMP) for the experiments (see Fig. 1a). The reservoir is connected to the filtration module with a valve for microgel sample injection in between. By adding a thermal flow sensor (FIC) (Elveflow MFS4) to the setup and connecting it to the pressure controller, the filtration experiments could be executed with constant flux or constant pressure. The filtration module consists of a 3D-printed top and a bottom part (see Fig. 1b). In between, a polyethersulfone (PES) membrane (Pieper Filter GmbH) with a membrane area of $3.2\,\mathrm{cm^2}$ and a pore size of $100\,\mathrm{nm}$ was placed with two sealings. The top part of the cell features a ribbed structure where the membrane was placed later as support structure to prevent membrane deformation during the filtration experiments.

Before the membrane was placed in the filtration module, it was soaked in an equivolume mixture of water and ethanol for 24 h. A pure water permeability (PWP) was measured at 8 equidistant pressure steps, ranging from 0 to $70\,\mathrm{mbar}$ and calculated to $3284.44\,\mathrm{L\,m^{-2}\,h^{-1}\,bar^{-1}}$. A total amount of $1\,\mathrm{mg}$ of microgels in solution were injected to deposit a monolayer of microgels on the membrane. The corresponding pressure stepping protocol was similar to one used for determining the PWP with 8 equidistant pressure steps. Then, the foulant layers were removed by opening the cross-flow valve at volumes flows of $1000\,\mathrm{\mu L\,min^{-1}}$ for 5 min. Additionally, the membrane was extracted from the filtration cell and rinsed under water. With this procedure, we ensure sufficient cleaning from residual polymers. These once filtrated membranes with a monolayer of microgels on top were then used for one batch of experiments at constant conditions (n = 3), e.g. $1\,\mathrm{mg}$ and $100\,\mathrm{\mu L\,min^{-1}}$. In between repeating experiments with the same conditions, the membrane was cleaned again by opening the cross-flow valve and then rinsing it in water. If the experimental conditions were altered, a new membrane was used for these experiments and prepared as described above. To remove air bubbles trapped in the filtration cell high pressures exceeding the maximal TMP of the following experiment were applied to remove the bubbles. Only at bubble-free conditions the experiment was initiated.

For Fig. 2, a certain amount of particle suspension was injected into the injection valve in front of the module, depending on the experiment. As the three types of injected particles were stored in different concentrations, we calculated the injected mass for each particle type to enable comparison in their filtration performance. Depending on the experiment, the injected volume was adjusted to realize different foulant mass. The respective pressure/flux is set on the pressure controller, and the measurement is started. The microgels accumulate on the filter cake and the flux decreases/TMP increases. Meanwhile, the solvent is recirculated and percolates the filter cake resulting in a dead-end filtration with subsequent percolation of solvent. For the flux stepping experiments, the target flux is set to $200\,\mathrm{\mu L\,min^{-1}}$ (37 LMH) after the injection of $1\,\mathrm{mg}$ of the pNIPAM microgel solution. The flux was further increased by consecutive $50\,\mathrm{\mu L\,min^{-1}}$ steps up to a peak flux of $400\,\mathrm{\mu L\,min^{-1}}$ (74 LMH) and step-wise decreased to $200\,\mathrm{\mu L\,min^{-1}}$ (37 LMH). In a second cycle, this procedure was repeated up to a flux of $400\,\mathrm{\mu L\,min^{-1}}$ (74 LMH). Each flux step was held for $15\,\mathrm{min}$. The experimental protocol for the pressure stepping experiments was similar with an initial target and peak pressure of $200\,\mathrm{mbar}$ and $400\,\mathrm{mbar}$, respectively. Each pressure step lasted $10\,\mathrm{min}$.

The flux was set to $200\,\mathrm{\mu L\,min^{-1}}$ (37 LMH) for experiments with varied total injected microgel mass in Fig. 3. The resistance of the clean membrane without foulant was interpolated based on the PWP measurements for the flux value of $200\,\mathrm{\mu L\,min^{-1}}$ to $9.75\,\mathrm{mbar}$. Polystyrene particles (PS) were not included in Fig. 3a as no reasonable TMP could be detected at $200\,\mathrm{\mu L\,min^{-1}}$ as the resistance of the filter cake was significantly lower compared to the soft material systems. When the flux was varied, a constant amount of $1\,\mathrm{mg}$ of particle solution was injected for filtration. To visualize the low TMP of the PS particles in Fig. 3b as well, the amount of particles had to be increased by a factor of 7.5.

2.3. Confocal microscopy analysis and Fourier transform

To visualize the filtration process, the height, and the development of the filter cake, a modified filtration module including a $175\,\mathrm{\mu m}$ thick cover glass on the bottom part was used (see Fig. 4a) such that the filter cake during filtration can be observed in-situ via laser scanning confocal microscopy (Leica TCS SP8). For online imaging, a 63x air objective was used for imaging slices of the filter cake in the x/y plane at a resolution of 1024 × 1024 and a 10x air objective in the x/z plane at a resolution of 2048 × 2048.. The chosen resolution and the applied scan speed resulted in approx. $5\,\mathrm{s}$ per image. The emission wavelength was set to $559\,\mathrm{nm}$.

Based on the x/z slices, the filter cake thickness was measured over time for every image. As the contrast between the fluorescing filter cake and the weakly fluorescing bulk is high, measuring the filter cake thickness could be automated by a Matlab script. The data were smoothed by a Gaussian function with a smoothing factor of 200. For the x/y slices, a 2D Fourier transform was performed to calculate the interparticle distances. A Gaussian fitting was used to determine the peak in the characteristic particle distance in the hexagonal arrangement

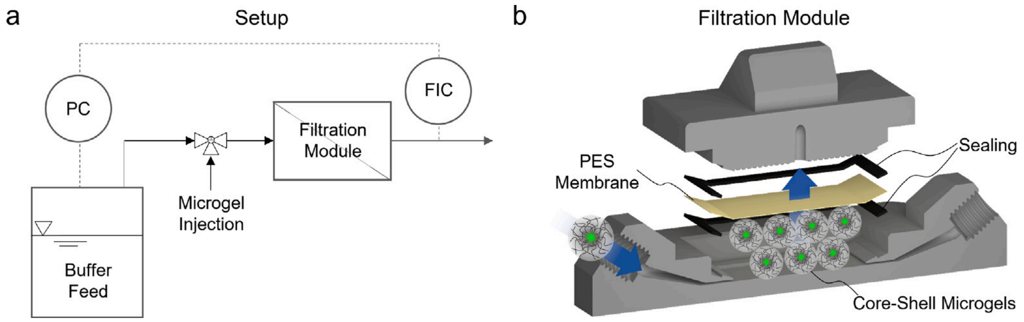

Fig. 1. (a) Experimental setup for dead-end filtration of pNIPAM microgels with PS core at a PES membrane in (b) an additive manufactured filtration module.

of the microgels in the filter cake for each image. In total, the filter cake was scanned in 39 time steps with 18 images in z-direction each, resulting in an approximate duration of the experiment of 45 min. A Gaussian smoothing taking the last 7 data points into account was used for plotting the particle distances over time in specific layers with a distance of 30 μm.

2.4. Bubble pressure measurements and centrifugation

The permeate is collected every 2 min during filtration of 1 mg of pNIPAM microgels at 200 $\mu L\,min^{-1}$. For the bubble pressure measurements (Krüss BP100), air is bubbled through a capillary with a diameter of 0.346 mm. The surface age is tracked in a logarithmic manner in a range from 10 ms to approx. 300 000 ms with 5 data points between each power of ten. To compare the purification performance, the microgel solution was purified by an ultracentrifuge (Optima XPN-80, Beckmann-Coulter) at 30,000 rpm for 1.5 h at room temperature. In total, the microgel solution was purified in 7 cycles. After each cycle, the supernatant was removed by pipetting and analyzed via bubble pressure tensiometry. The remaining sediment was diluted in double-distilled water, mixed with a roller mixer overnight at room temperature for redispersion and centrifuged for the next cycle.

2.5. NMR

Nuclear magnetic resonance (NMR) spectroscopy measurements were conducted at a frequency of 400 MHz and at room temperature (Bruker Avance III). As the polymer concentration was low, several samples of the permeate (collected during the first 10 min of filtration) were mixed. Additionally, the clear identification of multiplets due to the low concentration was not possible. For comparison, the permeate after 10 to 20 min was also collected to compare the polymer concentration at the beginning of the filtration with the steady-state. The water was evaporated by a rotary evaporator for both samples, and the residues were diluted in deuterated water. Poly(N-isopropylacrylamide):^{1}H NMR (D_2O, 400 MHz): δ 8.35 (1H), 3.79 (1H), 2.29 (1H), 1.23/1.45 (2H), 1.04 (2H).

2.6. AFM

Samples for the atomic force microscopy (AFM) measurements were prepared by drop casting. Therefore, rectangular pieces of ultra-flat silicon wafers were cleaned in an isopropanol ultrasonic bath, dried, and treated in an ozone oven (UVC-1014, NanoBioAnalytics, Germany) for 15 min. Subsequently, 100 μL of the respective microgel solution was dripped onto an activated substrate and the substrate was allowed to dry for several hours prior to measurement. AFM measurements were performed on a dimension icon AFM in closed-loop operation (Veeco Instruments Inc., USA, Software: NanoScope 9.4, Bruker Co., USA). Images of the microgels were recorded in tapping mode using OTESPA tips (NanoAndMore USA Corp., USA) with a nominal tip radius smaller than 7 nm, a nominal spring constant of 26 N/m and a nominal resonance frequency of 300 kHz. Images were corrected using Gwyddion (version 2.65) [44]. The height profiles for untreated and filtered microgels were measured in Gwyddion software. Mean values and standard deviations were calculated from height profiles of 10 different microgels from each batch. Each microgel was measured twice, with both measurement lines being perpendicular. To estimate the volume of dried microgels at the interface, at least 24 microgels were individually extracted from AFM images of size 20 × 20 μm^2 with a resolution of 512 × 512 pixels. Each segmented image was corrected by employing a linear background subtraction based on the pixels at the edges of the image. The volume of the microgels $V_{h,sum}$ was then calculated from the sum of the height values of each pixel h_i multiplied by the area per pixel A_{px} according to equation

$$V_{h,sum} = A_{px} \sum_{i=1} h_i \tag{1}$$

The threshold to distinguish between the background and polymer of the microgel shell was set to 6 nm.

3. Results and discussion

3.1. Resistance fluctuations

In this study, we filtered soft pNIAPM microgels in dead-end operation with subsequent percolation of water at either constant flow or pressure, with flow or step functions and varied the amount of filtered microgels as well as the flux level.. For constant flux filtration in Fig. 2a, 1 mg of microgel solution was injected into the system via a valve in front of the filtration module. During the first minutes of dead-end operation, microgels accumulate on top of the membrane, leading to an expected increase in TMP. As the cake layer's build-up is complete and no further microgels reach the filter cake, water percolates the obtained filter cake and a steady-state should be reached after time and a constant TMP is expected. However, after a steep increase, the TMP peaks at 830 mbar after 11 min, followed by a decline to 466 mbar until a steady-state is reached. This decline of 56% indicates an unexpected reduction in resistance of the accumulated filter cake. Flux and pressure stepping experiments were conducted to examine this phenomenon at different compression levels. In Fig. 2b, we increased the flux in five consecutive flux steps for 15 min each. Similar to the constant flux experiment, the TMP peaks at 4 min in the first flux step after starting the measurement and declines afterward. The flux was then decreased to the initial level in 5 steps before a second flux-stepping cycle was initiated. During the second flux-stepping cycle, the TMP decrease continues until a steady-state is reached in the second flux-stepping iteration. The TMP remains constant for each flux step at repeated flux increase in the second iteration. We expand the observations on this reduction in resistance by increasing the pressure step-wise instead of the flux (see Fig. 2c). Each step is held for 10 min. After insertion of the microgels, the flux drops to a minimum after 7 min due to particle deposition on the membrane surface. Similar to the findings before, the

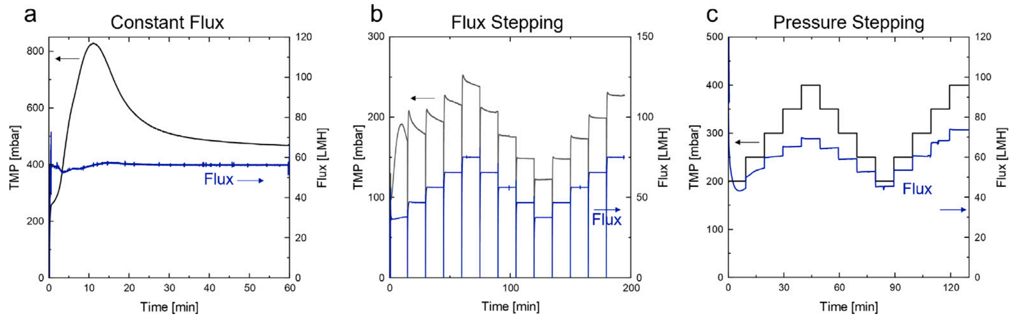

Fig. 2. TMP and flux curves for experiments at (a) constant flux, (b) flux stepping and (c) pressure stepping experiments.

overall resistance then declines, and the flux, in turn, increases until a steady-state is reached after 3 to 4 pressure steps. No flux increase during each step is observed at a second pressure stepping iteration. Both flux and pressure stepping experiments indicate that once the steady-state is reached, the resistance of the filter cake remains constant over time.

Overall, we report a reproducible decrease in resistance during the start-up procedure when filtrating soft pNIPAM microgels at different filtration conditions indicating severe changes in the filter cake properties.

3.2. *Variation of total injected microgel mass, flux and sample material*

To further describe the effect of resistance decrease during the start-up of filtration, we investigated the influence of the total injected microgel mass and the set flux level on the resulting peak and the steady-state pressure. In addition to the microgels, we filtrated a second soft particle system made from carbopol and, in contrast, solid polystyrene particles to compare the influence of the particles' softness on the resistance decrease.

We varied the mass of injected particle solution from 0.5 to 2 mg and kept the flux constant to 200 μL min^{-1} (37 LMH) for 60 min to ensure steady-state conditions. In Fig. 3a, the peak and steady-state pressures are given for each total injected microgel mass. The resistance of the clean membrane was neglected as its share to the overall TMP was measured to 10 mbar at 200 μL min^{-1} (37 LMH) in PWP measurements. As the total injected microgel mass increases, the TMP and, thus, the hydraulic resistance of the filter cake increase. On top, the phenomenon of resistance fluctuation is amplified for higher injected microgel mass by the increasing difference of peak to steady-state pressure. Although these differences are in the range of error bars ($n = 3$), the increase in permeability from peak to steady-state pressure is evident in every experiment. Due to the soft nature of the particles and their deformation at elevated TMP, the correlation between TMP and flux as well as TMP and injected mass is not linear. With increasing injected mass and increasing filter cake thickness the particles compress and deform, reducing filter cake porosity and increasing the hydraulic resistance. It is assumed that the first particle layers at the membrane feature the highest compression with the lowest void space in the filter cake and mainly contribute to overall hydraulic resistance of the overall filter cake [16]. For carbopol particles as a second soft material system, the peak and steady-state pressures, and hence, the filter cake resistances increase at higher total injected microgel mass as well. However, the difference between peak and steady-state pressure in Fig. 3a is less pronounced compared to the microgel system. No decrease in pressure could be identified for the solid PS particles. In addition, the resistance of the PS particles was not distinguishable from the resistance of the clean membrane with about 10 mbar at comparable total injected microgel mass and fluxes and has been excluded from this graph. Since a distinct resistance reduction is an artifact soft particle filtration only, we can exclude the filtration module causing this phenomenon.

In Fig. 3b, we injected a constant amount of 1 mg and measured the pressure at different flow rates. As reported in the graph previously, TMP, hydraulic resistance and the difference between peak and steady-state pressure are highest for the microgel system. With increasing flux, the microgels deform and narrow the inter-particle voids, as already reported previously [16], yielding high hydraulic resistances and an increasing pressure decrease from peak to steady-state. Comparably to Fig. 3a, the second material system from carbopol shows a less pronounced decrease in resistance between both pressure states and lower absolute pressures. As the hydraulic resistance of the filter cake from 1 mg of PS particle solution was not distinguishable from the PWP measurements of the clean membrane 7.5 times more particles had to be injected to be able to detect a hydraulic resistance of the filter cake from PS particles. This illustrates the influence of particle deformation and the resulting pore narrowing during filtration of soft particles on the hydraulic resistance of the filter cake. For solid particles, the TMP-flux relationship is nearly linear in Fig. 3b with only minor deviation. We attribute the deviation from linearity to an inhomogeneous filter cake thickness over the length of the filtration module due to the lateral injection the module. In addition, the system reached a steady-state without a pressure peak and subsequent decrease to a steady-state, showing that the phenomenon described in this study is an attribute of soft matter filtration only. With increased total injected microgel mass and flux, this pressure decrease amplifies for both soft material systems tested.

Plotting the ratio of steady-state to peak TMP over the total injected particle mass and flux in Fig. 3c indicates that the relative resistance fluctuations for carbopol particles are even greater than for microgels. One possible explanation for this behavior could be that the carbopol particles exhibit a higher Young's modulus compared to the microgels. This suggests that the carbopol particles are less elastic, which results in a reduced narrowing of the void spaces in the filter cake and consequently, a lower resistance and TMP level. The observed greater relative differences between peak and steady-state TMP further support this hypothesis, indicating a higher degree of degradation of the carbopol particles compared to the microgels, despite the fact that the shear stresses experienced by the carbopol particles is lower due to larger pores. However, this speculative explanation requires further studies on the degradation of carbopol particles in agglomerations under shear.

The increasing error bars at increased injected particle mass and the variations of the TMP ratio over the flux are an artifact of the experimental setup used in this work. During the experiments, the flux was held constant using a pressure controller, which took several seconds to achieve the target flux level asymptotically. This gradual increase was necessary to avoid flux overshoot, which could further compact the filter cake, increase hydraulic resistance, and result in higher TMPs, complication comparisons due to varying compression histories of soft materials [30]. Higher injected microgel masses and set flux levels made it more difficult to quickly regulate at the desired flux level constantly without overshooting or fluctuations in the regulating pressure. At 2 mg injected microgel mass, only one filtration experiment

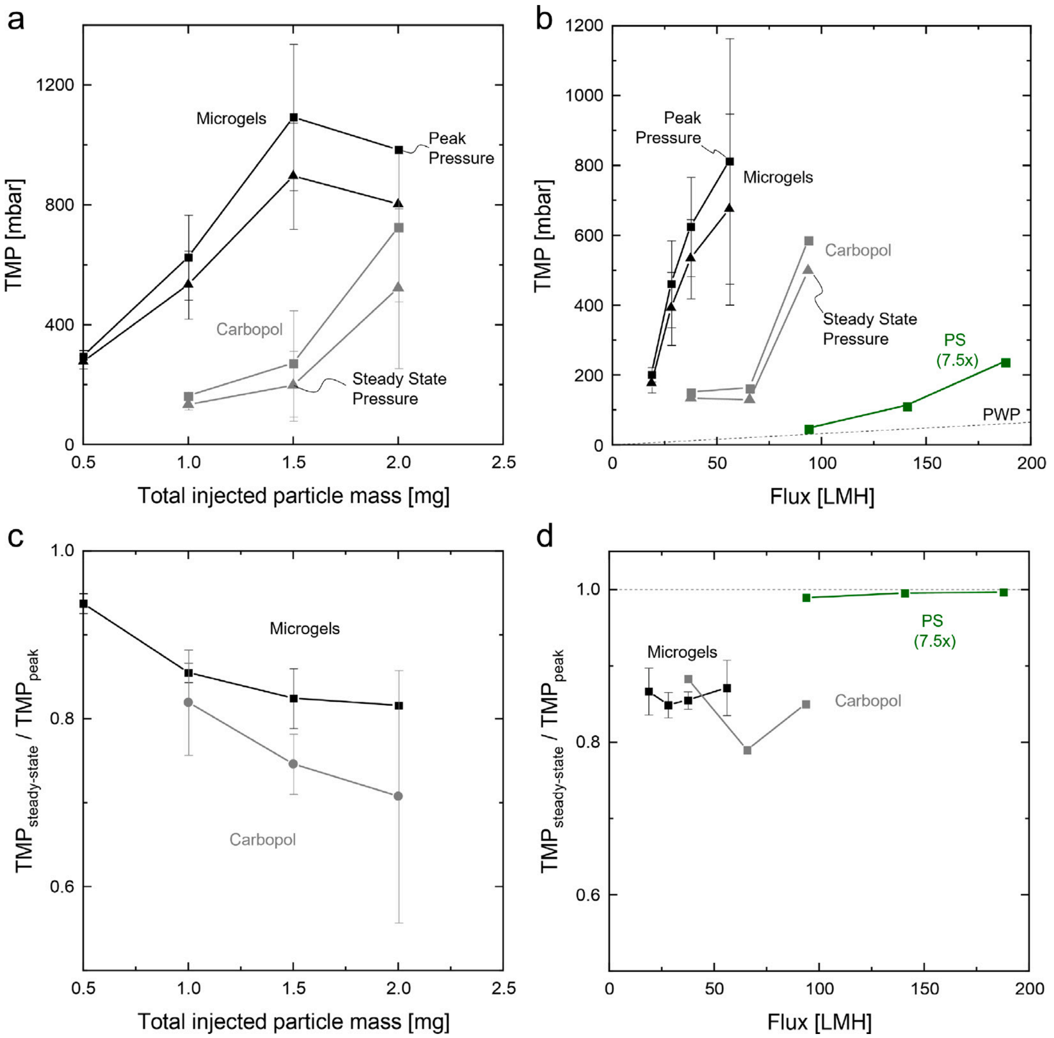

Fig. 3. Peak ■ and steady-state pressures ▲ visualized for microgels (black), carbopol (gray) and PS particles (green) at (a) different total injected microgel mass in solution for $200\,\mu\mathrm{L}\,\mathrm{min}^{-1}$ (37 LMH) and (b) varied fluxes with the same injected mass in each experiment of 1 mg. For the PS particles, a 7.5 times higher particle mass was taken. The ratios of steady-state to peak pressure are plotted for varied total injected particle mass (c) and varied flux (d). (For interpretation of the references to color in this figure legend, the reader is referred to the web version of this article.)

could be performed under the specified conditions. Fig. 3d further illustrates that the observed resistance fluctuations are a perquisite of soft material filtration only. However, a direct correlation between relative TMP and flux is not identified.

3.3. Cake build-up and particle distances

The previously described reduction in resistance and TMP during the start-up of the filtration of up to 56% indicate substantial structural shifts within the filter cake. Due to particle deformation at higher TMPs, the particle fraction can exceed the theoretical limit for densely packed spherical and solid particles of 0.74 [45,46]. In order to visualize the structural shifts inside the filter cake, the filtration module was slightly adapted, and a cover slip was glued to the bottom part (see Fig. 4a). This modification enabled in-situ observations and analysis of the membrane surface and the accumulating filter cake during dead-end filtration by confocal microscopy.

Images of the x/z plane show a cross-section of the filter cake, unraveling the development of the filter cake thickness over time (see Fig. 4b). The microgels' cores with a diameter of 200 nm are labeled with a fluorescent dye, indicating the position of the microgels as tiny dots in the images. In addition, this cross-section offers the possibility to determine the point in time at which no microgels remain in the bulk and all microgels accumulate in the filter cake. The visualization of the x/y plane in Fig. 4c enables a detailed description of the particle distances inside a specific layer of the filter cake over time.

With the adapted filtration module, we were able to correlate the filter cake thickness to the decrease in filter cake resistance observed in pressure/flux measurements. The dotted line and the gray area in Fig. 4d indicate the filter cake thickness during filter cake build-up at a constant flux of $200\,\mu\mathrm{L}\,\mathrm{min}^{-1}$. In the first minutes of the filtration, the pressure increases as the filter cake grows over time. At about 8 min, the pressure peaks at about 350 mbar and declines after several minutes to 330 mbar. This decline, however, does not coincide with the end of the filter cake build-up. Based on the x/z confocal microscopy images, we can determine that after about 14 min, all injected microgels accumulated on top of the membrane, and no additional microgels reach the cake. However, the filter cake thickness further increases over time due to a reswelling of the filter cake as the TMP decreases. The independently decreasing resistance of the filter cake in perspective to

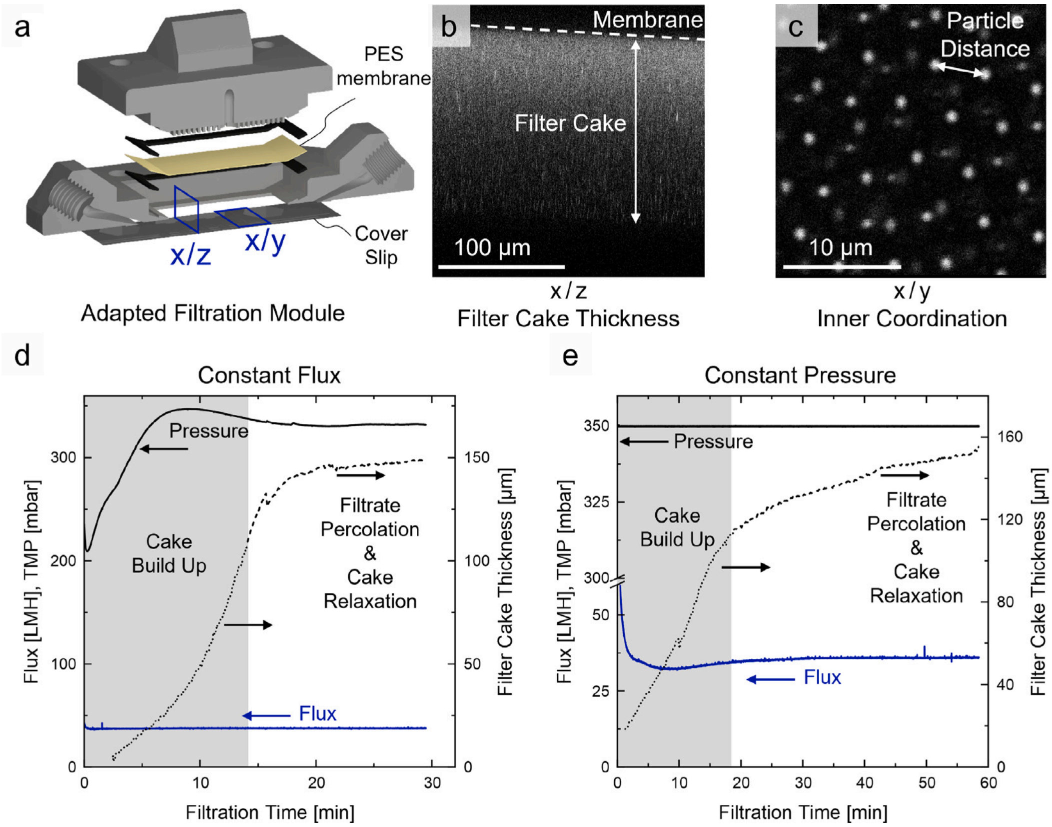

Fig. 4. Visualization and analysis of the filter cake for microgel filtration using confocal microscopy in a (a) dead-end filtration cell suitable for in-situ observation of the membrane surface during the filtration experiment. Confocal microscopy allows (b) x/z visualization of the filter cake's cross-section and (c) x/y visualization of the filter cake. Only the microgel cores are labeled. The filter cake thickness is measured using the x/z data and (d) plotted with the filtration flux and pressure for a constant flux and (e) a constant pressure filtration. The dotted curves correspond to the time when the feed consists of a microgel solution and the filter cake grows by inflowing microgels. The dashed lines correspond to the time when the feed consists only of a buffer solution without inflowing microgels.

the cake build-up is also visible when performing constant pressure experiments (see Fig. 4e). The flux decreases to a minimum at about 9 min and slightly increases during cake build-up. Besides, an almost constant cake relaxation can be observed in this experiment.

In conclusion, the confocal microscopy observations describe two overlapping but opposing effects during the filtration. On the one hand, the resistance initially increases due to a growing filter cake by depositing microgels. On the other hand, a reduction in TMP/increase in flux displays a reduction in resistance leading to cake relaxation by changes in shape and volume of the microgels in the filter cake. Once all microgels accumulate in front of the membrane, the latter phenomenon of resistance reduction due to microgel reswelling and reshaping and the coupled cake relaxation dominates.

We expand the in-situ description of the filter cake during filtration by scanning the cake in multiple x/y observation planes with an inter-plane distance of about 30 µm during constant pressure filtration. The images show the fluorescent particle cores of 0.2 µm of the microgels, which have an overall diameter of 1.9 µm (see Fig. 4c). From these images, the mean inter-particle distance at observation planes with constant distances to the membrane z are determined by a 2D Fourier transform. As the filter cake is compressed at higher TMPs, the soft shells of the microgels deform, the microgels shrink, and the particle distances decrease. In return, the filter cake porosity decreases resulting in a higher resistance of the filter cake. As illustrated in the x/y scan in Fig. 4c, the particles partly self-assemble into a hexagonal packing featuring a characteristic inter-particle distance at higher TMPs as previously described by Linkhorst et al. for microgel filtration. [47]. The crystallinity enables the microgel packing to be analyzed by a 2D Fourier transform of the images to calculate the mean particle distance in specific observation planes at a constant distance to the membrane z. These inter-particle distances in the filter cake are plotted in Fig. 5a for the specific observation planes over time, enabling an in-situ description of the filter cake morphology during the filtration. However, the further away a microgel layer is from the membrane, the more randomly the inter-particle distances are distributed and an analysis using 2D Fourier transform becomes inaccurate and error-prone. For comparison, the flux during the constant pressure filtration and the duration for the filter cake build-up are illustrated at higher magnification in Fig. 5b.

Overall, Fig. 5a shows that with increasing distance from the membrane *z*, the inter-particle distance also increases, indicating highly compressed layers directly at the membrane. In these layers, the inter-particle distances are only 1/3 of the particles' diameter demonstrating high particle deformation and compression and small voids between the particles. As the void's radius correlates to the pressure loss by the power of four (Hagen–Poiseuille), the first compressed layers have a significant share to the overall filter cake's hydraulic resistance. In contrast, the layers further away from the membrane are less compressed and more loosely packed as already observed by Epstein et al. during alginate filtration [48].

As already described for Fig. 4, two effects now overlap. Firstly, the hydraulic resistance increases due to the filter cake build-up and the

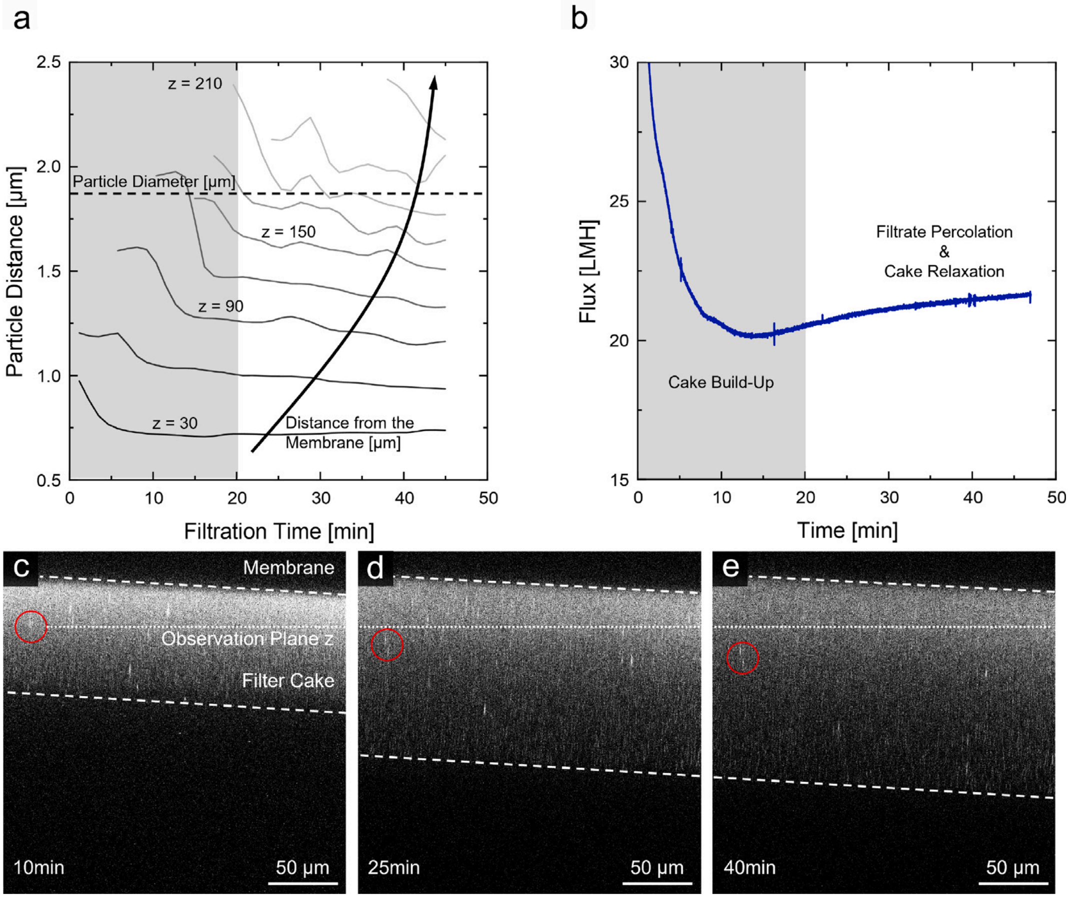

Fig. 5. (a) Filter cake density displayed as inter-particle distance during a constant pressure filtration of microgels at 350 mbar over time. The inter-particle distances are shown for specific observation planes with a constant distance from the membrane z. The graph results from a 2D Fourier transform of x/y images as illustrated in Fig. 4c. (b) Corresponding flux during filtration sectioned in cake build-up (gray) and cake relaxation (white). The x/z planes show the filter cake thickness at specific points in time for (c) 10 min, (d) 25 min and (e) 40 min of filtration from a different experiment. The dotted line represents the static observation plane with a constant distance from the membrane and the red circle a brighter microgel that moves away from the membrane during filtration.

deformation of the particles. This is demonstrated by a sharp decline in inter-particle distances in Fig. 5a for different z values. Secondly, the phenomenon of reduced resistance leads to a reswelling of the filter cake. This effect starts to dominate after about 13 min, the point of maximum resistance. For the interpretation of the particle distance curves over time, it must be taken into account that the observation planes are at a constant position with constant distances to the membrane while the reswelling microgel layers move away from the membrane. Over time, a specific observation plane of e.g. z=30 µm, displays several different microgel layers. In addition, the movement of microgel layers away from the membrane is more pronounced for layers near the bulk as the reswelling effect accumulates along the layers toward the bulk.

We underlined our interpretation of Fig. 5a by adding an x/z image sequence over time with highlighted filter cake thickness from a different experiment. The red circles in Fig. 5c–e indicate two bright and recognizable microgel cores that increase their distance from the membrane during the experiment and thereby passing several observation planes. The complete image sequence is given as supplementary video in Appendix C.

Based on the particle distance measurements, a link between microscopic events during filtration and macroscopic filter cake and filtration behavior can be made, revealing much higher compression in the first layers of the filter cake compared to the layers being more distant to the membrane. Additionally, the reswelling of microgel layers due to the phenomenon of resistance reduction leads to a movement of microgel layers away from the membrane. However, the in-situ observation could not reveal the cause for the relaxation and the decrease in hydraulic resistance.

3.4. Comparison of purification techniques

Microgels necessitate a robust purification process following their synthesis to remove undesired side products and residuals. These contaminants primarily consist of monomer residues, surfactants used in the reaction, and linear pre-polymers that form as byproducts. These molecules are considerably smaller than the targeted microgels, so their removal can be achieved effectively through membrane processes such as ultrafiltration or dialysis. Ultracentrifugation offers an alternative purification method and is often preferred for concentrating microgel solutions. Ensuring sufficient purification is vital to obtain microgels with the desired properties and functionalities, free from impurities that might interfere in future usage.

We investigated the influence of the purification step on the decrease in filtration resistance by additionally purifying the microgel solution via 7 cycles of ultracentrifugation and comparing subsequent filtration performance at constant flux. Compared to the filtration lacking the additional centrifugal purification, the TMP reaches a steady-state after several minutes without a decrease in resistance. On top,

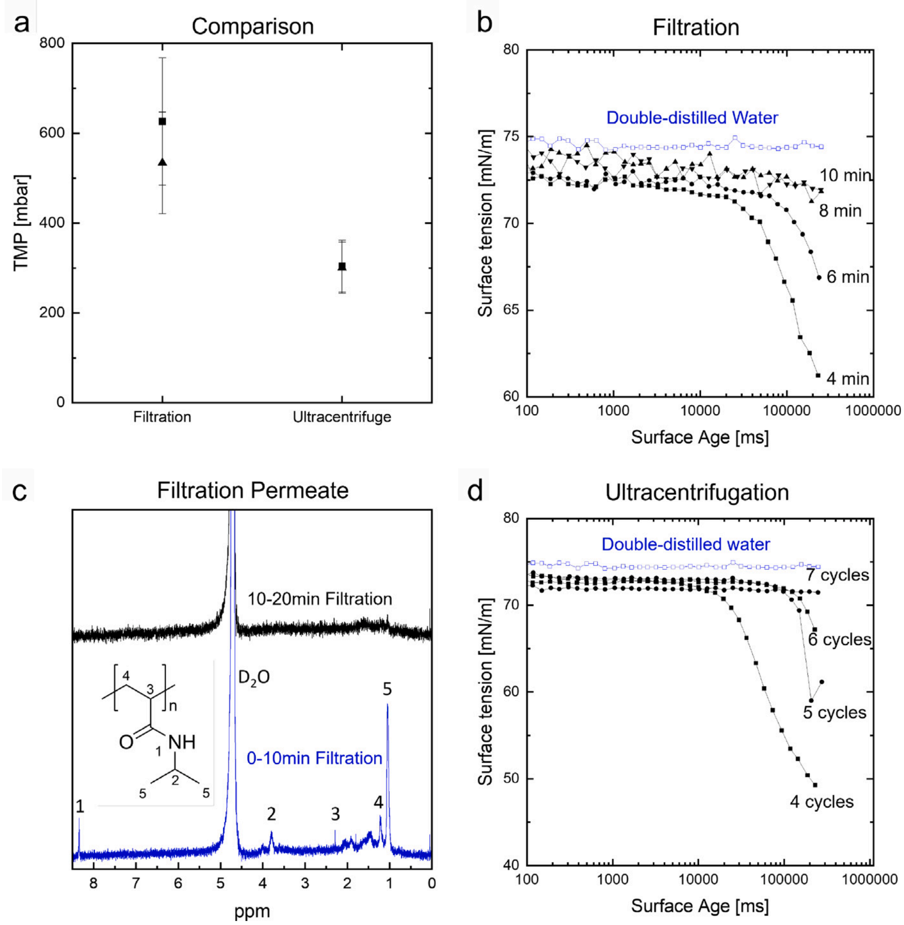

Fig. 6. (a) Comparison of peak ■ and steady-state pressures ▲ for the first filtrations at 200 μL min^{-1} (37 LMH) and 1 mg of microgel solution for a single dead-end filtration and a filtration with purified microgels by seven cycles in an ultracentrifuge beforehand. (b) Bubble pressure tensiometry measurements of the permeate during a first filtration of dialyzed microgels and (d) of the supernatant after several cycles of ultracentrifugation prior filtration (reprinted with permission from [49]). (c) NMR analysis of the permeate during the first 10 and 10–20 min of filtration of dialyzed microgels in D$_2$O.

the steady-state TMP is reduced by about a half to 301 ± 57 mbar instead of 534 ± 113 mbar (see Fig. 6a), clearly indicating an influence of the purification technique on the filtration performance. At this point, we assume polymer chains to be washed out of the filter cake during filtration, leaving voids in the cake, which leads to the decreased hydraulic resistance described previously. By additional purification with the ultracentrifuge, polymer chains are removed from the solution beforehand, thus, leading to an expected filtration behavior which reaches a steady-state without any resistance fluctuations.

To strengthen this assumption, additional monitoring of the permeate's surface tension over time by bubble pressure tensiometry was performed. Bubble pressure tensiometry gauges the surface tension of a bubble at different surface ages, mirroring the affinity of surface-active molecules to the air–water interface. Accordingly, it serves as an analytical tool to assess the presence of high-molecular-weight polymers in a liquid. Fig. 6b illustrates the surface tension at different surface ages of the permeate for microgels purified via dialysis only. At the beginning of the filtration at 4 min, the surface tension decreases at higher bubble surface ages, indicating the presence of surface-active polymer chains in the permeate. The surface tension of the permeate increases during filtration until it reaches a steady-state after about 10 min. At this stage, no surface-active polymer chains are present in the permeate as the surface tension is close to the value of water at room temperature. In subsequent NMR analysis of the permeate (Fig. 6c), the surface-active substances were identified to be pNIPAM. However, calculating a detailed concentration over time was not possible due to the low concentration of pNIPAM in the permeate.

Furthermore, the bubble pressure tensiometry of the supernatant for each ultracentrifugation cycle indicates residues of polymer after multiple centrifugation cycles (Fig. 6d). A complete purification of the microgel solution from polymer chains could be achieved after seven cycles. For the subsequent filtration of the microgels, no polymer chains are released from the filter cake, the void size in the filter cake is maintained, and the TMP reaches a steady-state without any hydraulic resistance decrease.

However, the origin of the polymer chains remains yet unknown. Two plausible explanations account for the presence of dissolved polymer chains in the microgel solution. First, the polymer chains are linear pre-polymers that originated from the synthesis process and were not sufficiently removed during dialysis. They accumulated in the filter cake and were subsequently washed out. Alternatively, the observed polymer chains result from degradation of the low crosslinked polymer shell, which are caused by shear force of the permeating flow through the filter cake voids [32].

In Fig. 7, atomic force microscopy (AFM) images were taken to investigate the structural integrity of the microgels before and after filtration. As all microgels were dialyzed in advance, the untreated microgels after dialysis serve as reference. In addition, height profiles

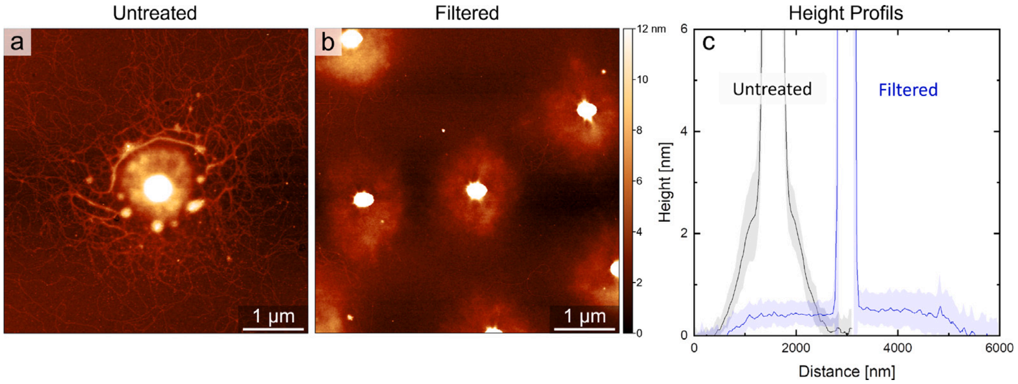

Fig. 7. AFM images of the microgels (a) untreated after dialysis (and before filtration) and (b) after filtration. (c) illustrates a magnification of the height profiles for both microgel batches (n = 10).

for both microgel batches are added to Fig. 7. The untreated microgels exhibit a smaller shell-diameter in comparison to the filtered microgels. However, the polymer is higher concentrated at the core and in the inner parts of the shell as compared to the filtered microgels. While the filtrated microgels' shell is barely distinguishable from the background at heights below 1 nm, the shell of the untreated microgels reaches heights of over 2 nm. In addition, the core of the untreated microgels features a slightly wider core which might be attributed to a higher density of pNIPAM at the immediate vicinity of the PS-core. Furthermore, single polymer chains are more clearly visible and branch out more widely in comparison to the filtered microgels in Fig. 7b. Overall, the filtered microgels illustrate more evenly distributed polymer in the microgel's shell and a flatter shell compared to the untreated microgels. However, volume integrating of the AFM topographic data over the whole microgel revealed a 22% higher volume for the filtered microgels compared to the untreated microgels when spreading on a solid interface. We attribute the increased volume observed for the filtered microgels in the AFM images to a decrease in polymer density, which is caused by individual bond rupture events within the low crosslinked polymer network of the shell. The drag forces exerted during filtration induce the cleavage of covalent bonds, causing polymer fragments to permeate toward the downstream as indicated in literature [32]. This reduction of polymer density softens the polymer network and facilitates the spreading of the shell on the wafer surface in the AFM images resulting in a larger radius for the filtered microgels in Fig. 7c. Regarding the condition within the filter cake, the removal of shell material can result in either an increased shell porosity or a reduced microgel size. In both cases, the pores within the filter cake become larger, which could explain the phenomenon of a reduction in resistance.

In conclusion, the AFM images illustrate a degradation of the microgel shell for force-intensive purifications, such as dead-end filtration and ultracentrifugation. In contrast to alternative purification methods like dialysis, filtration and ultracentrifugation involve substantially higher forces, thereby elevating the probability for degradation of the soft microgel shell. While filtration offers advantages in scaling up purification capacity after the microgel production, the potentially altered microgel properties necessitate careful consideration. The observed shell degradation in dead-end filtration agree with the findings of Izak-Nau et al., who correlated polymer network degradation to the cleavage of covalent bonds in the network upon shearing [32]. Polymer chains are ruptured during filtration and permeate through the filter cake. The change in mass either leads to an increase polymer porosity or a reduction in shell diameter and the permeability of the overall filter cake increases, leading to the observed reduction in resistance. However, further studies are necessary to elucidate to what extent polymer chains rupture from the polymer network, to what extent residual polymer chains from the synthesis contribute to the effect of resistance reduction, and how the degradation influences the single microgel softness.

Furthermore, the fact that core–shell microgels degrade during filtration should be considered when applying them as model particles in filtration studies. However, degrading microgels as a model system may be helpful to understanding and investigating analogous observations in resistance fluctuation during the start-up procedure of filtrations in practical filtration applications. In addition, this study underscores the intricate nature of soft matter filtration and suggests an additional contributing factor to the overall filter cake resistance: the degradation of the colloidal matter. Besides filtration studies, the varying microgel integrity and properties depending on the purification technique could have noteworthy implications for other applications involving shear forces.

4. Conclusions

This study combines a lab-scale dead-end filtration setup, core–shell microgels as soft model particles and microfluidic visualization techniques to investigate an unexpected resistance decrease during the filtration start-up procedure. This effect was observed in different process conditions, such as constant flux, constant pressure, flux and pressure stepping, at different amounts of filtrated microgels, and for different constant fluxes. AFM images illustrate a degraded shell after filtration, and bubble pressure tensiometry combined with NMR analysis confirms the presence of polymer chains in the permeate within the initial minutes of filtration. We deduce that applying substantial shear forces to the microgels' shell during filtration leads to the rupture of polymer chains from the low-density polymer network. These ruptured chains then permeate through the filter cake and membrane, creating voids in the filter cake and consequently diminishing its hydraulic resistance. These observed amplifications of the reduction in hydraulic resistance at elevated flux rates are attributed to an increased shear force and an enhanced degradation of the microgel shell. With higher particle mass, more layers accumulate in front of the membrane, increasing the TMP, and enhancing the resistance reduction effect due to a greater amount of residual polymers being washed out. During filtration, confocal microscopy unveiled cake relaxation caused by a reduction in resistance due to the permeation of chains, increasing porosity in the filter cake. This relaxation of the cake occurs during the whole process of filtration and superimposes with the initial resistance increase during cake build-up.

This study underscores the impact of microgel shell degradation involving shear stress, particularly in filtration applications. It highlights the necessity of considering the potentially altered properties of microgels when used as model particles in filtration studies. Further studies with integrated optical force probes [50] could elucidate the degree of microgel shell degradation during filtration in more detail. Overall, this investigation highlights the complexity inherent in soft matter filtration, introducing the integrity of the filtered material as an additional factor influencing overall filter cake resistances.

CRediT authorship contribution statement

Lucas Stüwe: Writing – review & editing, Writing – original draft, Visualization, Validation, Supervision, Project administration, Methodology, Investigation, Formal analysis, Data curation, Conceptualization. **Arne Lüken:** Writing – review & editing, Visualization, Validation, Supervision, Project administration, Methodology, Investigation, Formal analysis, Data curation, Conceptualization. **Felix Stockmeier:** Methodology, Formal analysis, Data curation. **Lukas Griesberg:** Investigation, Formal analysis, Data curation. **Timon Kratzenberg:** Writing – original draft, Investigation, Formal analysis, Data curation. **John Linkhorst:** Writing – review & editing, Supervision, Resources, Project administration, Methodology, Funding acquisition, Conceptualization. **Walter Richtering:** Writing – review & editing, Supervision, Resources, Project administration, Methodology, Funding acquisition, Conceptualization. **Matthias Wessling:** Writing – review & editing, Supervision, Resources, Project administration, Methodology, Funding acquisition, Conceptualization.

Declaration of competing interest

The authors declare that they have no known competing financial interests or personal relationships that could have appeared to influence the work reported in this paper.

Data availability

Data will be made available on request.

Acknowledgments

Lucas Stüwe and Arne Lüken contributed equally to this work. This work was funded by the Deutsche Forschungsgemeinschaft (DFG, German Research Foundation) - 514031987. The authors wish to acknowledge support via the Deutsche Forschungsgemeinschaft through the collaborative research center SFB 985 “Functional microgels and microgel systems” - 191948804. M.W. acknowledges funding by the Deutsche Forschungsgemeinschaft through the Gottfried Wilhelm Leibniz Award 2019 (WE 4678/12-1) and appreciates the support from the Alexander-von-Humboldt foundation. The authors like to thank Alexander Petrunin for his support in bubble pressure measurements, Lea Greie for NMR analysis, and Frédéric Grabowski, Lea Steinbeck and Sebastian Rauer for their fruitful discussions.

Appendix A. Microgel size distributions

The microgel size distribution in Fig. A.8 was measured via DLS and reveals a mean diameter of about 1.9 μm. The higher variations at large diameters is attributed to agglomerations of microgels.

Appendix B. Full AFM height profiles

To illustrate that the cores of the microgels with a diameter of approx. 200 nm are significantly larger than the variations in thickness of the shell of the microgels, the complete height profile from Fig. 7c for untreated and filtered microgels was added in Fig. B.9 for the sake of completeness.

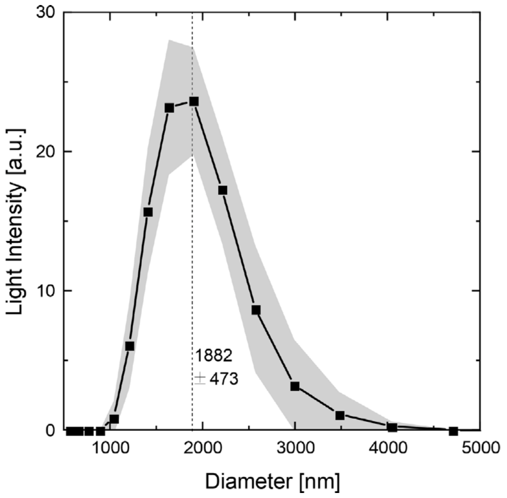

Fig. A.8. Size distributions of microgel used in this work measured by DLS.

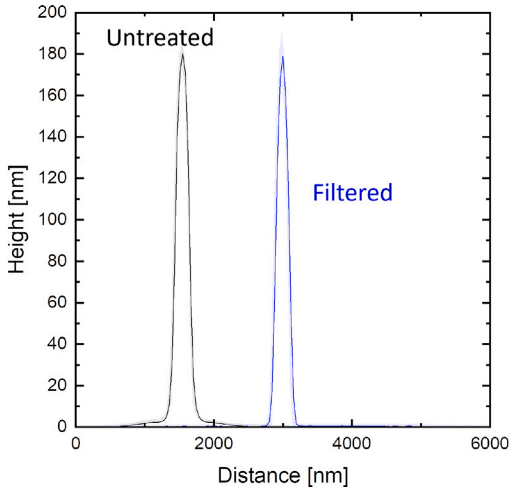

Fig. B.9. Full height profile of untreated and filtered microgels from Fig. 7c at full scale.

Appendix C. Filter cake relaxation

The supplementary video is the complete image sequence of the x/z plane shown in Fig. 5c-e taken over 329 images within a time frame of 57 min. The brightness of the image sequence was adjusted to better visualize the filter cake thickness. After about 18 min the filter cake is build up and all microgels accumulated on the membrane. However, an increase in filter cake thickness is still visible indicating filter cake swelling. The size of the image sequence is about 250 × 250 μm.

Supplementary material related to this article can be found online at https://doi.org/10.1016/j.memsci.2024.122988.

References

[1] D.M. Warsinger, S. Chakraborty, E.W. Tow, M.H. Plumlee, C. Bellona, S. Loutatidou, L. Karimi, A.M. Mikelonis, A. Achilli, A. Ghassemi, L.P. Padhyek, S.A. Snyder, S. Curcio, C.D. Vecitis, H.A. Arafat, J.H. Lienhard V, A review of polymeric membranes and processes for potable water reuse, Progr. Polymer Sci. 81 (2018) 209–237.

[2] D. Zhao, J.U. Barrientos, Q. Wang, S.M. Markland, J.J. Churey, O.I. Padilla-Zakour, R.W. Worobo, K.E. Kniel, C.I. Moraru, Efficient reduction of pathogenic and spoilage microorganisms from apple cider by combining microfiltration with UV treatment, J. Food Protect. 78 (4) (2015) 716–722.

[3] G. dos Santos Bernardi, J. Dal Magro, M.A. Mazutti, J.V. Oliveira, M. Di Luccio, G.L. Zabot, M.V. Tres, Microfiltration for filtration and pasteurization of beers, in: Engineering Tools in the Beverage Industry, Elsevier, 2019, pp. 405–434.

[4] M.R. Zaheer, A. Gupta, et al., Current development and future perspectives of microbial enzymes in the dairy industry, in: Enzymes in Food Biotechnology, Elsevier, 2019, pp. 287–302.

[5] A. Rathore, A. Shirke, Recent developments in membrane-based separations in biotechnology processes, Preparative Biochem. Biotechnol. 41 (4) (2011) 398–421.

[6] I. Bouhid de Aguiar, K. Schroën, Microfluidics used as a tool to understand and optimize membrane filtration processes, Membranes 10 (11) (2020) 316.

[7] J. Lohaus, Y. Perez, M. Wessling, What are the microscopic events of colloidal membrane fouling? J. Membr. Sci. 553 (2018) 90–98.

[8] B. Bräsel, S.-W. Yoo, S. Huber, M. Wessling, J. Linkhorst, Evolution of particle deposits at communicating membrane pores during crossflow filtration, J. Membr. Sci. 686 (2023) 121977.

[9] F.M. Tiller, J.H. Kwon, Role of porosity in filtration: XIII. Behavior of highly compactible cakes, AIChE J. 44 (10) (1998) 2159–2167.

[10] I. Griffiths, P. Stewart, A hybrid discrete–continuum framework for modelling filtration, J. Membr. Sci. 647 (2022) 120258.

[11] H. Hamedi, O. Mohammadzadeh, S. Rasouli, S. Zendehboudi, A critical review of biomass kinetics and membrane filtration models for membrane bioreactor systems, J. Environ. Chem. Eng. 9 (6) (2021) 106406.

[12] K.-H. Choo, C.-H. Lee, Membrane fouling mechanisms in the membrane-coupled anaerobic bioreactor, Water Res. 30 (8) (1996) 1771–1780.

[13] J. Hermia, Constant pressure blocking filtration laws: Application to power-law non-Newtonian fluids., Trans. Inst. Chem. Eng. (60) (1982) 183–187.

[14] E. Giraldo, M. LeChevallier, Dynamic mathematical modeling of membrane fouling in submerged membrane bioreactors, in: WEFTEC 2006, Water Environment Federation, 2006, pp. 4895–4913.

[15] C.W. MacMinn, E.R. Dufresne, J.S. Wettlaufer, Large deformations of a soft porous material, Phys. Rev. Appl. 5 (4) (2016) 044020.

[16] J. Linkhorst, J. Rabe, L.T. Hirschwald, A.J. Kuehne, M. Wessling, Direct observation of deformation in microgel filtration, Sci. Rep. 9 (1) (2019) 18998.

[17] G. Foley, A review of factors affecting filter cake properties in dead-end microfiltration of microbial suspensions, J. Membr. Sci. 274 (1–2) (2006) 38–46.

[18] J.W. Chew, J. Kilduff, G. Belfort, The behavior of suspensions and macromolecular solutions in crossflow microfiltration: An update, J. Membr. Sci. 601 (2020) 117865.

[19] J. De Jong, R.G.H. Lammertink, M. Wessling, Membranes and microfluidics: A review, Lab Chip 6 (9) (2006) 1125.

[20] I.S. Ngene, R.G. Lammertink, M. Wessling, W. Van Der Meer, A microfluidic membrane chip for in situ fouling characterization, J. Membr. Sci. 346 (1) (2010) 202–207.

[21] G.C. Agbangla, É. Climent, P. Bacchin, Experimental investigation of pore clogging by microparticles: Evidence for a critical flux density of particle yielding arches and deposits, Separ. Purif. Technol. 101 (2012) 42–48.

[22] M. Wessling, Two-dimensional stochastic modeling of membrane fouling, Separ. Purif. Technol. 24 (3) (2001) 375–387.

[23] P. Bacchin, Q. Derekx, D. Veyret, K. Glucina, P. Moulin, Clogging of microporous channels networks: role of connectivity and tortuosity, Microfluidics Nanofluidics 17 (2014) 85–96.

[24] N. Debnath, A. Kumar, T. Thundat, M. Sadrzadeh, Investigating fouling at the pore-scale using a microfluidic membrane mimic filtration system, Sci. Rep. 9 (1) (2019) 10587.

[25] I. Bouhid de Aguiar, M. Meireles, A. Bouchoux, K. Schroën, Conformational changes influence clogging behavior of micrometer-sized microgels in idealized multiple constrictions, Sci. Rep. 9 (1) (2019) 9241.

[26] D.A. Holden, G.R. Hendrickson, W.-J. Lan, L.A. Lyon, H.S. White, Electrical signature of the deformation and dehydration of microgels during translocation through nanopores, Soft Matter 7 (18) (2011) 8035–8040.

[27] D.A. Holden, G. Hendrickson, L.A. Lyon, H.S. White, Resistive pulse analysis of microgel deformation during nanopore translocation, J. Phys. Chem. C 115 (7) (2011) 2999–3004.

[28] M.G.R. Hendrickson, L.A. Lyon, Microgel translocation through pores under confinement, Ang. Chem. (Int. Ed. English) 49 (12) (2010) 2193.

[29] J. Linkhorst, J. Lölsberg, S. Thill, J. Lohaus, A. Lüken, G. Naegele, M. Wessling, Templating the morphology of soft microgel assemblies using a nanolithographic 3D-printed membrane, Sci. Rep. 11 (1) (2021) 812.

[30] A. Lüken, L. Stüwe, J. Lohaus, J. Linkhorst, M. Wessling, Particle movements provoke avalanche-like compaction in soft colloid filter cakes, Sci. Rep. 11 (1) (2021) 12836.

[31] A. Aufderhorst-Roberts, D. Baker, R.J. Foster, O. Cayre, J. Mattsson, S.D. Connell, Nanoscale mechanics of microgel particles, Nanoscale 10 (34) (2018) 16050–16061.

[32] E. Izak-Nau, D.E. Demco, S. Braun, C. Baumann, A. Pich, R. Göstl, Shear-induced structural and functional transformations of poly (n-vinylcaprolactam) microgels, ACS Appl. Polymer Mater. 2 (4) (2020) 1682–1691.

[33] A. Lüken, M. Bruckhaus, U. Kosfeld, M. Emondts, M. Wessling, Automated tangential-flow diafiltration device, HardwareX 10 (2021) e00200.

[34] S. He, S. Schog, Y. Chen, Y. Ji, S. Panitz, W. Richtering, R. Göstl, Photoinduced mechanical cloaking of diarylethene-crosslinked microgels, Adv. Mater. 35 (41) (2023) 2305845.

[35] K. Rietema, Stabilizing effects in compressible filter cakes, Chem. Eng. Sci. 2 (2) (1953) 88–94.

[36] E. Tarleton, S. Morgan, An experimental study of abrupt changes in cake structure during deadend pressure filtration, Trans. Filtration Soc. 4 (1) (2001) 93–100.

[37] F.M. Mahdi, T.N. Hunter, R.G. Holdich, A study of cake filtration parameters using the constant rate process, Processes 7 (10) (2019) 746.

[38] D. Büning, F. Ennen-Roth, T. Netke, J. Schumacher, M. Ulbricht, Microfiltration of polymeric microgels as soft model colloids through sterile filter membranes, J. Membr. Sci. 649 (2022) 120364.

[39] K.O. Messerian, A. Zverev, J.F. Kramarczyk, A.L. Zydney, Characterization and associated pressure-dependent behavior of deposits formed during sterile filtration of mRNA-lipid nanoparticles, J. Membr. Sci. 684 (2023) 121896.

[40] D. Go, T.E. Kodger, J. Sprakel, A.J. Kuehne, Programmable co-assembly of oppositely charged microgels, Soft Matter 10 (40) (2014) 8060–8065.

[41] A. Lüken, J. Linkhorst, R. Fröhlingsdorf, L. Lippert, D. Rommel, L. De Laporte, M. Wessling, Unravelling colloid filter cake motions in membrane cleaning procedures, Sci. Rep. 10 (1) (2020) 20043.

[42] Z. Jaworski, T. Spychaj, A. Story, G. Story, Carbomer microgels as model yield-stress fluids, Rev. Chem. Eng. 38 (7) (2022) 881–919.

[43] E. Di Giuseppe, F. Corbi, F. Funiciello, A. Massmeyer, T. Santimano, M. Rosenau, A. Davaille, Characterization of carbopol® hydrogel rheology for experimental tectonics and geodynamics, Tectonophysics 642 (2015) 29–45.

[44] D. Nečas, P. Klapetek, Gwyddion: an open-source software for SPM data analysis, Open Phys. 10 (1) (2012) 181–188.

[45] L.A. Lyon, J.D. Debord, S.B. Debord, C.D. Jones, J.G. McGrath, M.J. Serpe, Microgel colloidal crystals, J. Phys. Chem. B 108 (50) (2004) 19099–19108.

[46] H. Bachman, A.C. Brown, K.C. Clarke, K.S. Dhada, A. Douglas, C.E. Hansen, E. Herman, J.S. Hyatt, P. Kodlekere, Z. Meng, et al., Ultrasoft, highly deformable microgels, Soft Matter 11 (10) (2015) 2018–2028.

[47] J. Linkhorst, T. Beckmann, D. Go, A.J. Kuehne, M. Wessling, Microfluidic colloid filtration, Sci. Rep. 6 (1) (2016) 22376.

[48] J.A. Epstein, G.Z. Ramon, In-situ micro-rheology of a foulant layer at a membrane surface, J. Membr. Sci. 640 (2021) 119747.

[49] A.C. Lüken, G. Ramon, M. Wessling, From soft matter filtration processes to microfluidic filter cake visualization (Ph.D. thesis), Chemical Process Engineering, RWTH Aachen University, GER, 2022, http://dx.doi.org/10.18154/RWTH-2022-11194.

[50] C. Baumann, M. Stratigaki, S.P. Centeno, R. Göstl, Multicolor mechanofluorophores for the quantitative detection of covalent bond scission in polymers, Ang. Chem. Int. Ed. 60 (24) (2021) 13287–13293.